Study of the evolution of transport properties induced by additive processing sand mold using X-ray computed tomography

Saptarshee Mitra[1], Mohamed EL Mansori[1,2], Antonio Rodríguez de Castro[3], Marius Costin[4]

[1]*Laboratoire MSMP – EA7350, Arts et Métiers ParisTech, 2 Cours des Arts et Métiers, 13617 Aix-en-Provence, France*

[2]*Texas A&M Engineering Experiment Station, College Station, TX 77843, USA*

[3]*Laboratoire MSMP – EA7350, Arts et Métiers ParisTech, Rue Saint Dominique, 51006 Châlons-en-Champagne, France*

[4]*CEA, LIST, Department of Imaging & Simulation for Non-Destructive Testing, F-91191 Gif-sur-Yvette, France*

Abstract

Accurate characterization of the mass transport properties of additively processed sand molds is essential in order to achieve reproducibility of the produced castings and control of gas defects in foundry industries. The present work highlights the potential use of X-ray micro-computed tomography (µ-CT) to characterize the evolution of permeability and some major microstructural features of such additively processed sand molds. The evolution of mass transport properties of sand mold samples under specific processing conditions met in additive manufacturing and its influence on the porosity, the permeability, the tortuosity, and the pore and throat size distributions were characterized from 3D images provided by X-Ray µ-CT. The obtained results showed that the mass transport properties of additively processed sand molds can be closely predicted by using non-destructive in situ methods, such that improvements to the casting can be made to create more optimized 3D printed structures for foundry applications.

Keywords: Additive manufacturing; 3D-printed casting sand mold; Permeability; Pore Size Distribution; X-ray µ-CT; Numerical simulations; Pore network modeling.

1. Introduction

Three-Dimensional Printing (3DP) technology, also termed as Additive Processing (AP) or joining technology, emerged as a new rapid manufacturing method in foundry industries to build three-dimensional (3D) sand molds directly from Computer-Aided Design (CAD) models in layers. As compared with the traditional conventional sand mold, (Sachs et al., 1990) stated that this kind of rapid-prototyping technique offers the ability to efficiently

manufacture sand molds and cores in casting industry with optimized geometries as designed with CAD without the need of extensive molding. Additively processed sand mold is also advantageous over conventional methods due to its ability to reduce surface defects in the molds as shown by (Hawaldar and Zhang, 2018). Rapid prototyping technique has been accepted extensively in the casting industries due to its proven capability to reproduce a virtually complex designed object into a real casting mold. (Almaghariz, 2015) studied the economic advantage of 3DP technology and found that there is no influence of part complexity on the manufacturing costs of molds and cores. This technique allows the production of highly complex components in a cost-effective way as shown by (Almaghariz et al., 2016) and good surface finish as shown by (Hawaldar and Zhang, 2018). Despite being still limited in number, the applications of AP technique are much diversified, including aerospace, automobile, and medical industries. Consequently, 3DP represents a step forward towards autonomous casting in which a sand mold can be printed without any machining stage. In this regard, (Upadhyay et al., 2017) published an extensive literature review elsewhere, so only the key features of additively processed sand molds are reminded in the present article.

AP has enabled the casting industries and foundries to produce more complex sand molds without using any kind of physical model, through a succession of thin layer which are directly generated from 3D CAD files. The layer-based rapid prototyping technology, or Powder Binder Jetting (PBJ), consists in bonding individual particles with a liquid resin binder, which generates porous parts. The existence of such porosity is necessary in casting sand molds so that the gases can be efficiently evacuated from the mold cavity through the interstices during filling of the mold. This minimizes the risk of casting defects caused by gas trapping in the liquid alloy. Fig. 1(a) describes the PBJ process, in which ceramics kind of

materials are generally used as to provide refractoriness to the mold, and a liquid resin binder provides cohesion in between such ceramic particles by forming capillary bridges, Fig. 1(b). For metal casting, a temperature-resistant material is required, so silica sand is generally used as granular material for the PBJ process, and a furan resin is commonly taken as a liquid binder due its high performance in terms of dimensional accuracy and mechanical strength of the printed mold. Also, various 3D printing process parameters directly affect the quality of the sand mold. In particular, the relationship between the printing process parameters (print position/orientation in job-box, recoater speed, and print resolution) and their influence on the properties of the 3DP sand mold have been extensively investigated in previous works using both mathematical modelling by (Coniglio et al., 2017) and experimental validations by (Sivarupan et al., 2017). (Sivarupan et al., 2017) showed how the printing processing parameters affected mechanical properties in 3DP sand mold. It was also reported by (Mitra et al., 2019) that the mechanical strength and permeability of 3DP sand molds are deeply dependent on the amount of binder and the ageing conditions. In this regard, the evolution of permeability and mechanical strength of such additively processed silica sand molds during curing was studied in a recent work by (Mitra et al., 2018) for different binder contents and curing parameters, showing that the 3D printed sand molds could be stored for long time at room temperature before being used for metal casting, while no substantial variation in strength of 3DP mold was observed below 100 °C, the gas permeability was found to decrease with increase in curing temperature. However it is of equal importance for morphological characterization of such additively processed porous structures to be standardized in foundry with proven quality control, especially as the 3DP structures can be customized and changed (based on printing process parameters) easily to alter its mass transport properties based on casting requirements.

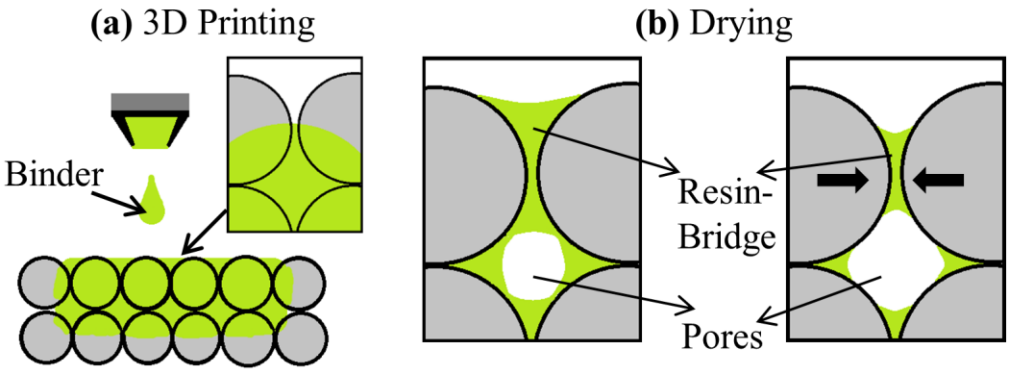

Fig. 1. The PBJ process showing, (a) the initial distribution of furan binder within the silica sand particles, (b) the drying stage of resin-bridges by infrared heating during the printing of the mold and the optional curing stage to obtain stronger resin-bridge after printing of the mold.

Characterization of mass transport properties through pore networks with complex geometry and connectivity, such as 3DP sand molds, is essential in order to assess the risks of incomplete filling and gas porosity in castings. The fundamental microstructural characteristics include grain size distribution, pore size distribution, throat (pore constriction) size distribution, pore-to-throat size ratio, pore connectivity, and tortuosity. These microscopic physical properties will control the macroscopic characteristics of the 3DP molds in terms of permeability and porosity governing the flow of liquid metal, and, more generally, the heat and mass transport within the 3DP sand mold. Therefore, knowledge of the relationships of 3DP process parameters and these microscopic characteristics is of vital importance to predict casting defects. On this subject, it was stated earlier by (Sivarupan et al., 2017) that high reacoater speeds lead to lower grain packing densities in 3DP molds (porosity depends on recoating speed). It is also known that high levels of sand compaction reduce permeability due to the decrease in volume available for fluid flow and the increase in specific surface of the interstices. Pore Network Modelling (PNM) offers a simple demonstration of

the complex pore structure and topology, but quiet more accurate than traditional bundle-of-capillaries model. In PNM the void phase is divided into a set of spherical pores connected by cylindrical throats. A complete review of PNM for porous geometries (pore network construction) has been studied elsewhere by (Xiong et al., 2016). (Huang et al., 2019) used PNM to extract the network of pores and the connected throats from a fibrous material to simulate two-phase flow. It was shown by (Degruyter et al., 2009) and (Degruyter et al., 2010) that the permeability can be predicted using the throat size distributions with the modified Archie's law.

In the industrial foundry processes, numerical simulations of mold filling and casting solidification are employed in order to optimize the part designs, reduce the manufacturing costs and prevent defect generation. However, the lack of accurate estimations of key inputs, e.g., local porosity, density, permeability, and strength, limits the usefulness of the obtained numerical results. Therefore, it is crucial to develop a non-destructive method to properly characterize 3DP sand molds in order to predict the relationships between process parameters and the inputs to such simulations. Other non-destructive methods include the traditional permeability test in which air is injected to the 3D printed sample (although they need sampling of the mold). Also, Scanning Electron Microscope (SEM) imaging could be considered as a suitable non-destructive method, but only 2D microstructural information can be extracted. Although Mercury Intrusion Porosimetry (MIP) is by far the most popular method for characterizing the pore size distribution of porous materials with pores in the range of 500 μm to 3.5 nm as stated by (Giesche, 2006), MIP experiments are not expected to work well on unconsolidated materials like 3D printed casting sands because the applied pressure damages the material and its void-structure. X-ray micro computed tomography (μ-CT) is a non-destructive and non-intrusive method as stated by (FLANNERY et al., 1987),

allowing the characterization of 3D printed sand mold specimens. On this regard, a complete review of X-ray µ-CT and its applications has been studied elsewhere by (De Chiffre et al., 2014). X-ray µ-CT has emerged as a powerful nondestructive technique (NDT) for the direct 3D characterization of complex porous geometries. (Hazlett, 1995) stated that the 3D images of the pore space, like those provided by X-ray µ-CT, can be used for direct computation of multiphase fluid flow and to reliably characterize permeability from the realistic digital images provided by this technique.

Different numerical methods exist for the simulation of creeping flow through porous media at the microscale, e.g., Finite Volume Method (FVM) and Lattice Boltzmann Method (LBM). (Jaganathan et al., 2008) used FVM to model fluid flow through the real microstructure of a fibrous mat to predict the permeability and compared them to various analytical expressions. (Soulaine, 2015) used FVM to perform a direct numerical simulation of fluid flow in a fully saturated porous media for the prediction of permeability from µ-CT image. (Thabet and Straatman, 2018) idealized a geometrical introduced to characterize small volume of packed sand in pore-level computations using YADE (Yet Another Development Engine) solver. In previous research by (Boek and Venturoli, 2010), it was proved that using LBM, to obtain permeability from a digital image is a reliable alternative to destructive traditional measurements. (Malaspinas et al., 2010) presented a novel lattice Boltzmann scheme to simulate viscoelastic fluid flows, and stated that LBM results were found to be in good agreement with analytical and other numerical results. In this sense, some works were performed earlier by (Degruyter et al., 2010) combining LBM and X-ray µ-CT for the calculation of permeability of volcanic pumices. (Kadauw, 2014) characterized the local density of sand mold using industrial computed tomography, and found good agreement with the experimental density of sand mold. Some typical results were reported recently by

(Sivarupan et al., 2018) for the use of X-ray µ-CT to characterize the additively processed porous structure like 3DP sand mold. (Anbar et al., 2019) used LBM to predict permeability from a computer-generated sphere packing, and to study the impact of sand compaction from the simulations. However, no other literature review exists tackling the particular case of permeability characterization of 3DP sand molds from µ-CT digital images using LBM and PNM.

The current work will describe an accurate and rigorous method to characterize the physical properties of such additively processed sand mold from the digital images provided by X-ray µ-CT. The first point of inquiry is, what is the real local permeability of 3D printed structure? To achieve that goal, a set of X-ray µ-CT experiments are first performed on additively processed silica samples with different silica grain sizes and binder percentage. The microstructural properties are secondly determined through the use of image analysis techniques and PNM. Then, LBM numerical simulations and analytical methods are used to predict the permeability of the samples, and the results are subsequently compared to experimental measurements provided by traditional techniques.

2. Materials and methods

2.1. Manufacturing process of 3DP sand mold specimen

The raw materials in the current experiments were silica sand and a furfuryl-alcohol-composed binder (furan resin binder) with a density of (1.1-1.2) g/cm³, as provided by

188 (ExOne, 2014). The silica sand particles used in the present experiments had a mean particle
189 diameter of 140 µm and 190 µm as specified by the supplier in (ExOne, 2013).

190

191 The samples were designed with NetFabb^{TM} software and subsequently converted to .stl
192 format. The designed samples were printed with an ExOne S-Print-Furan 3D printing
193 machine, over a job-box size of 800 × 500 × 400 mm^3. The process of 3D printing began by
194 adding sulfonic acid (0.18 wt% of the sand) with 8 kg of sand inside a mixing chamber. The
195 acid-activated sand mixture was then transferred to the re-coater. Successive layers of sand
196 grains were added and compacted over the build platform by means of a re-coater head.
197 Furfuryl alcohol binder was then gradually injected by the print head nozzle on top of these
198 compacted sand layer beds in order to bind them. The injected furan-resin-binder droplets
199 tend to form a coating layer over individual sand grains. This causes the resin-bonded sand
200 grains to crosslink with each other by forming a resin bridge between the sand grains. The
201 additive processing of resin-bonded sand in layers continued until the designed part is
202 fabricated. This resin bridge in between the sand particles hardens gradually, hence providing
203 strength to the printed mold.

204

205 For the X-ray CT analysis, 10 small-grain and 10 big-grain cylindrical samples with different
206 binder percentages were printed and named accordingly as provided in Table 1. A set of 20 (5
207 × 2 different binder content × 2 different grain size) cylindrical specimens were printed for
208 the experimental permeability measurements, with a diameter of 50 mm and height of 50 mm.

209

210

211

Table 1. 3DP specimens used for analysis

Sample	Binder content (wt%)	Average grain size (µm)
Small Grains with High Binder content (SGHB)	~2	140
Small Grains with Low Binder content (SGLB)	~1	140
Big Grains with High Binder content (BGHB)	~2	190
Big Grains with Low Binder content (BGLB)	~1	190

The choice of the binder percentages was based on the recommended values for binder contents (0.9% - 2%) reported in previous research by (Hawaldar and Zhang, 2018). The dimensions of the 3D printed parts for X-ray µ-CT tests were measured manually using Vernier caliper, with top height of 12 ± 0.02 mm, base height of 10 ± 0.02 mm, top diameter of 4 ± 0.02 mm and base diameter of 6 ± 0.02 mm, respectively (the uncertainty corresponds to 95% confidence interval), Fig. 2(d). The temperature of the 3D printing room was controlled at 25 ± 2 °C and the measured relative humidity of the room was 40 ± 10%. A detailed experimental investigation of the effects of mass transport improvement on mechanical strength of 3DP sand mold was presented in previous works by (Mitra et al., 2018), (Mitra et al., 2019) and (Ramezani Dana and El Mansori, 2019).

2.2. Volumetric reconstruction of 3DP mold via X-ray tomography

2.2.1. X-ray micro computed tomography: image acquisition and post-processing

In the present study, reconstructed 3D tomographic images of 3DP specimens were used to extract information on microstructural characteristics (grains, pores, porosity, tortuosity) and permeability through image analysis, PNM and LBM simulations. The X-ray µ-CT images were obtained at a facility of CEA LIST (NDT department). The X-ray equipment consists of a micro-focus X-ray generator, a flat panel detector, and a turn-table, situated in a large inspection cell which enables the addition of instrumentation for in-situ characterizations. The X-ray generator is a Viscom 225 kV (320 W) model with a micro-focus spot-size. The detector is a Perkin Elmer XRD0822 model having 1024 x 1024 pixels of 200x200 μm^2 in size, and the acquisitions were performed in a classical setup with a rotating sample (360°) and static source and detector positions. The optimum scan settings for the specimens were determined, obtaining 100 kVp, 60 µA, and 1 second exposure time. For each CT scan, a number of 900 projections were acquired, with an integration time of 1 second. The total acquisition scan was about 30 minutes. The scan facility uses a temperature controlled inspection cell and therefore the impact of temperature variations is considered negligible. The magnification factor was set to 40, which gives a voxel size of 5 μm^3 in the CT images. The reconstructions and preliminary analysis were performed by using VGSTUDIO MAX^{TM} commercial software at a facility of CEA LIST (NDT department). The setup is shown in Fig. 2 as well as the sample holder and the details of specimens.

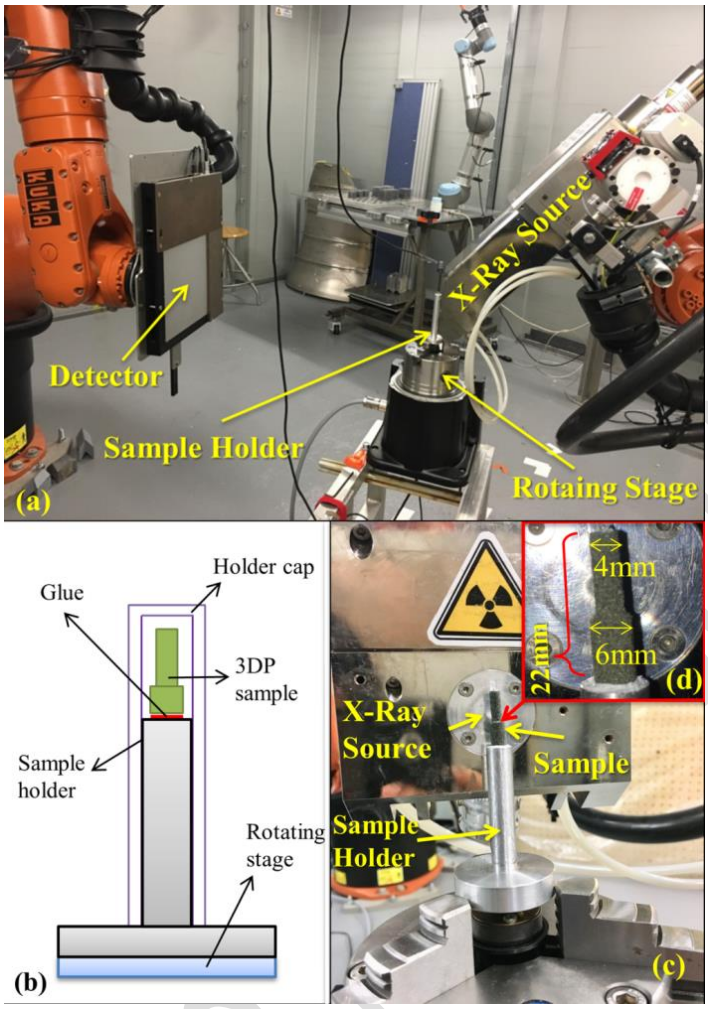

Fig. 2. Different views and schemes of the experimental X-ray µ-CT setup showing: (a) the robotic X-ray inspection platform, (b) a schematic design of the sample holder (c) the sample holder and (d) a zoom-in view including the dimensions of the sample.

For the morphological assessment of 3DP sand mold, the acquired 3D images were binarized and analyzed using the default algorithms provided by (Schindelin et al., 2012) included in ImageJ and subsequently post-treated using different software: ParaView by (Ayachit Utkarsh, 2015), PALABOS by (Latt J, 2009) and OPENPNM by (Gostick et al., 2016). The post-treatment procedure starts by cropping and scaling the raw stack of images, resulting in the cross-sectional dimensions displayed in Fig. 3. Reconstructed X-ray µ-CT images were then filtered using a variance weighted mean filter to reduce the effect of background noise. A

median filter of 2 voxels was applied, as shown in Fig. 3(b), to reduce noise without merging the solid particles. The cropped image was then binarized using the Otsu algorithm by (Smith et al., 2010) and was converted into an 8-bit greyscale thresholded image, as shown in Fig. 3(c). The reconstructed pixel data were then converted into an 8-bit grayscale image. It should be noted that a 3DP specimen consists of three phases with different attenuation coefficients: silica sand, resin binder and air (pores). It is to be noted that the binder produces a low contrast with respect to silica and is difficult to isolate in a CT image. Therefore, only two phases, e.g. void and solid, were identified in the present experiments. However, the absence of binder in the segmented image is not expected to significantly alter the computed permeability values, due to the low binder contents (1 – 2 wt%) and based on previous results as shown by (Mitra et al., 2019). Furthermore, the thresholding of the CT data was carried out in an iterative manner and validation of the threshold was performed through comparison of the estimated porosity to the porosity measured with a classical mass weighting apparatus.

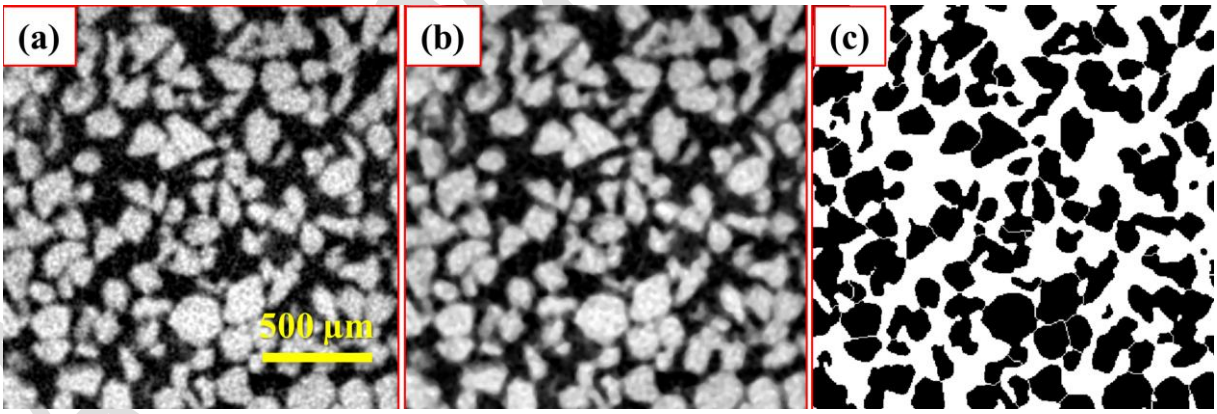

Fig. 3. Steps during post-treatment of the acquired images: (a) raw image (2D slice), (b) median filter treatment and (c) converted to 8-bit greyscale binary image. White represents interstices and black corresponds to solid grains in the binary image.

2.2.2. Grain size distribution and measurement of tortuosity

The sand grain shape and size plays an important role in the fabrication of 3DP sand mold, as they deeply impact the permeability of the sand molds, hence casting quality. The finer the silica grains, lower the permeability will be, similarly the coarse silica grains will lead to a higher permeability. Grains are generally categorized based on their shapes; rounded, sub-angular and angular. Rounded grains lead to high permeability of sand mold, due to least contact with other grains during the sand compaction. However, these kinds of grain shape do not pack up to its maximum, hence lacks strength. Whereas sub-angular grains have low permeability with high strength values compared to the rounded grains. The angular grain provides higher strength to the 3DP mold, but with low permeability due to tight packing of grains. Therefore it was of great importance to characterize the grain size distribution along with their forms, as it directly affects the casting quality.

For the analysis of the silica grains size distribution, Morpholib - Distance Transform Watershed 3D algorithm by (Legland et al., 2016) included in ImageJ was applied to the thresholded images in order to separate touching objects (creating a border far from the center of the overlapping object). The watershed segmentation algorithm detects and separates pore bodies in 2D or 3D images. Then, the connected components are scrutinized using Analysis 3D – Labelling plugin by (Boulos et al., 2013) from ImageJ. By using this algorithm, a new volume was generated in which all the particles were labeled. From the generated results, the equivalent diameter of each silica grain d_g was calculated using Eq. 1:

$$\mathrm{d}_g = \sqrt[3]{6 \times \mathrm{volmarch}/\pi} \tag{1}$$

with $volmarch$ being the volume in marching cubes. Then, a result file in .xl format was generated by using the Analysis 3D – Parameter plugin by (Boulos et al., 2013) listing several parameters: volume in pixel, volume in marching cubes, surface with marching cubes. A Granulometry-histogram plot was plotted using the total number of labeled particles as a function of particle diameter as obtained from Eq. 1. Then, the sphericity of the particles was computed using the following formula (nearly-spherical shapes approaching value 1):

$$\text{sphericity} = 6 \times \text{volmarch} \times \sqrt{\pi/\text{surfacemarch}^3} \quad (2)$$

Where $surfacemarch$ is the surface with marching cubes as shown by (Boulos et al., 2013). Furthermore, the porosity of the 3DP specimen was calculated by dividing summation of resulting $volmarch$ values by the size of the reconstructed image multiplied by total number of slices. Also, standard Kozeny–Carman equation (bundle of cylindrical capillaries model) was used to calculate permeability k from the obtained average grain diameter and pore space volume from the characterized µ-CT images by:

$$\text{k} = \frac{\varepsilon_{bed}^3 \, d_s^2}{180(1-\varepsilon_{bed})^2} \quad (3)$$

where ε_{bed} is the average porosity of the µ-CT images of the 3DP specimen and d_s is the average diameter of the silica grains.

To go further, the pore connectivity Z and the geometric tortuosity τ of the 3D printed sand mold specimens was also computed through an iterative-thinning algorithm (Median axis algorithm) by using Skeletonize 3D and Analyze Skeleton plugins from ImageJ by (Ignacio Arganda-Carreras et al., 2010) for all the 3DP specimens (SGLB, SGHB, BGLB, and BGHB). The number of branches that originate from a junction (3, 4 and >4 branches) is termed as pore connectivity, and the ratio between the regular and the Euclidean length of such branches is termed as geometric tortuosity. A result window from the plugin displays the node-to-node distances (d_i), Euclidian distances (d_{euclid}), total number of junctions (n_j), total number of triple-branch junctions (n_t), total number of quadruple-branch junctions (n_q). Any junctions above that is a high-order junctions (n_x). It was shown earlier by (Hormann et al., 2016), that the pore connectivity (Z) can be calculated from (n_j), (n_t), (n_q), and (n_x), using Eq. 4 and Eq. 5:

$$Z = 3\frac{n_t}{n_j} + 4\frac{n_q}{n_j} + 5\frac{n_x}{n_j} \tag{4}$$

$$\frac{n_x}{n_j} = 1 - \frac{n_t}{n_j} - \frac{n_q}{n_j} \tag{5}$$

Where, n_t/n_j, n_q/n_j, and n_x/n_j provides the fraction of nodes connecting 3, 4 and >4 branches respectively.

And the tortuosity was calculated as being the average ratio between node-to-node network distances (d_i) and Euclidean distances (d_{euclid}) as shown by (Ignacio Arganda-Carreras et al., 2010) and (Hormann et al., 2016):

$$\tau = \frac{1}{n}\sum_{i=1}^{n}\frac{d_i}{d_{euclid}} \tag{6}$$

The results in terms of pore connectivity (Z) and tortuosity (τ) are provided in Table 2. It can be observed that most junctions have 3 branches, a significant number of junctions have 4 branches and only a few present 5 or more branches. An average pore connectivity value of Z ≈ 3 is obtained. In this regard, (Sivarupan et al., 2018) showed in a previous work that the speed at which the recoater spreads the sand particles on the job box platform affects the pore-connectivity, hence affecting the permeability. It can be deduced from the results displayed in Table 2 that the size of the grain does not affect pore connectivity, in contrast to the case of recoating speed.

Table 2. Results from median axis algorithm, showing the pore connectivity and tortuosity

Sample	n_t/n_j	n_q/n_j	n_x/n_j	Pore connectivity (Z)	Tortuosity (τ)
SGHB	0.721	0.211	0.067	3.346	1.223
SGLB	0.703	0.243	0.052	3.348	1.221
BGHB	0.833	0.131	0.034	3.201	1.218
BGLB	0.773	0.176	0.049	3.275	1.225

2.3. Computational simulation of fluid flow in 3DP sand mold using Lattice Boltzmann Method

A volume of 367×367×367 voxel (corresponding to 1835×1835×1835 μm^3) was cropped from the original reconstructed image with voxels of 5^3 μm^3. The cropped image was then binarized using the procedure presented in subsection 2.2.1. The porosity was then computed by dividing the number of pore space voxels (white) by the total volume of the image stack.

The volume of the image being used as input to numerical simulations must be large enough to produce a representative and statistically meaningful value of permeability for the 3DP sand mold. While too big volumes would require a powerful and parallel computer clusters, the Representative Volume Element (RVE) must lead to statistically meaningful results while reducing computation time. Therefore, four different sizes of representative were selected from the original cropped binary image: 200×200×200 voxel, 150×150×150 voxels 100×100×100 voxels and 50×50×50 voxels, as shown in Fig. 4, corresponding to 1000×1000×1000 μm^3, 750×750×750 μm^3, 500×500×500 μm^3, and 250×250×250 μm^3 volumes, respectively. These 4 cropped segmented stacks were then used as inputs to the LBM numerical simulations performed with Lattice-Boltzmann Method (LBM) solver PALABOS in order to determine the RVE for permeability calculation. The entire process was repeated for all the binder content-grain size combinations listed in Table 1.

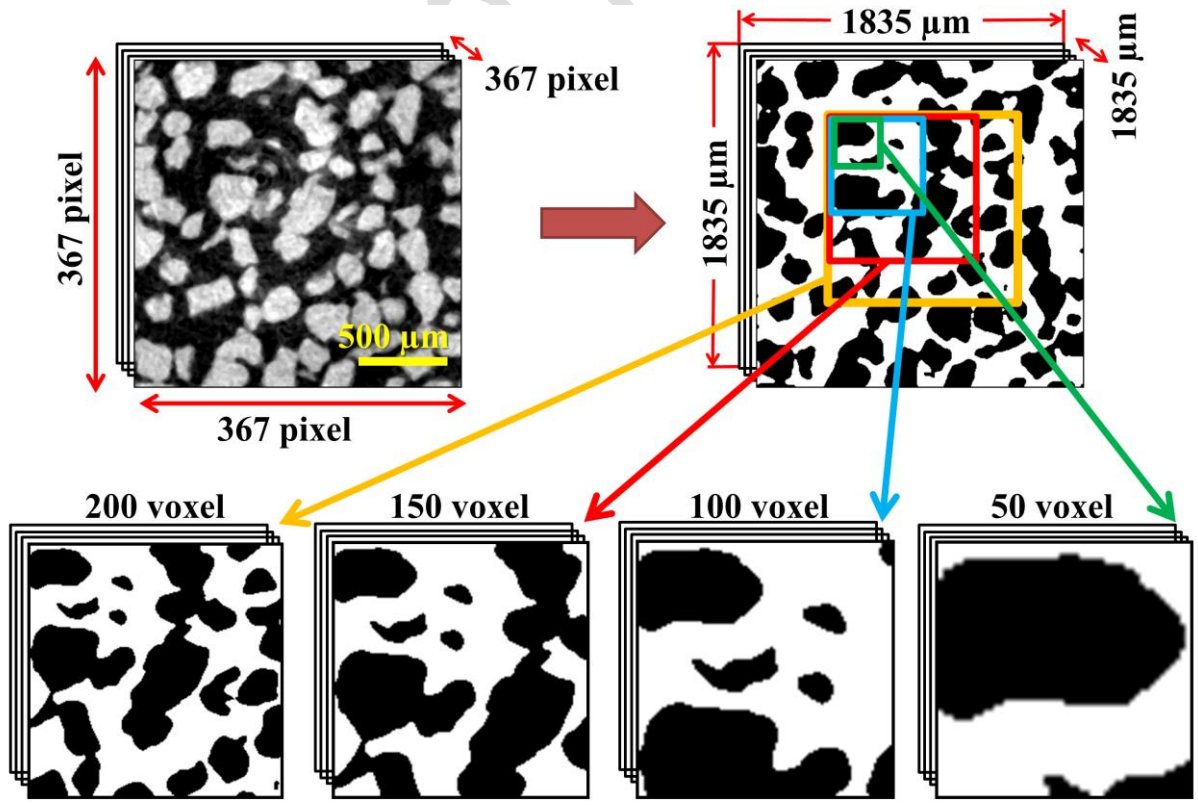

Fig. 4. Images of different dimensions used to determine the Representative Volume Element (RVE) of the BGLB specimen. Pores are displayed in white and silica sand grains in black on the binary image.

The numerical simulations were performed by using the open-source Lattice-Boltzmann Method (LBM) solver PALABOS (Parallel Lattice Boltzmann Solver). LBM is highly reliable and has been applied extensively as discussed by (Chopard B et al., 2002). (Heijs and Lowe, 1995) used LBM to predict the permeability of a random array of spheres and clay soil, and found that the predicted permeability is consistent with the experimentally measured values. (Ferrol and Rothman, 1995) studied the numerical simulations of mass transport through 3D tomographic images of Fontainebleau sandstone, and found that the LBM simulations were similar as compared to the finite difference calculations and with the laboratory experimental measurements. It was studied and verified earlier by (Auzerais et al., 1996) that X-ray micro computed tomography (µ-CT) along with LBM can be used for modeling the fluid flow phenomena through complex porous geometries to study the permeability. (Degruyter et al., 2010) combined X-ray µ-CT and LBM solver PALABOS to perform numerical simulations of gas flow through volcanic pumices, and validated the method by comparing the resulting data with the experimentally obtained values. Hence for the present numerical simulation, LBM was used to predict the permeability of the additively processed sand mold.

For the numerical simulation of mass transport through the 3D tomographic image of 3DP specimen, a bounce-back boundary condition (no-slip boundary condition) was applied in between the interfaces of pore space and silica sand grains. In PALABOS-LBM numerical

simulation, a D3Q19 lattice scheme is proposed as demonstrated earlier by (Hecht and Harting, 2008). D3Q19 lattice describes the fluid flow in three dimensions with 19 possible velocity vector directions, along with the zero velocity as shown by (Hecht and Harting, 2008) and (Ding and Xu, 2018). A standard Bhatnagar Gross-Krook (BGK) collision operator was applied to the D3Q19 lattice scheme. A constant pressure gradient (∇P) was applied through the porous medium, and the initial velocity within the interstices was set to zero. The imposed values of ∇P were low enough to ensure creeping flow regime (Darcy flow). Non-slip boundary conditions were applied and the lateral boundaries of the porous geometry shown in Fig. 5. Permeability (k) was then measured on the non-dimensional lattice unit system from the obtained pressure and velocity maps using Darcy's equation:

$$-\frac{dP}{dz} = \frac{\mu}{\mathrm{k}} v \tag{7}$$

where dP/dz is the pressure gradient along the main flow z-direction, μ is the dynamic viscosity, v is Darcy velocity and k is the permeability of the 3DP mold. The calculation methodology used by PALABOS to measure the permeability of porous media involves in solving a modified version of the actual Darcy's equation. Here, *Q/A* is denoted by the term v, which is the mean fluid velocity through the porous media or as stated earlier as Darcy's velocity. Q is the flow rate of fluid through a sample of cross section area A.

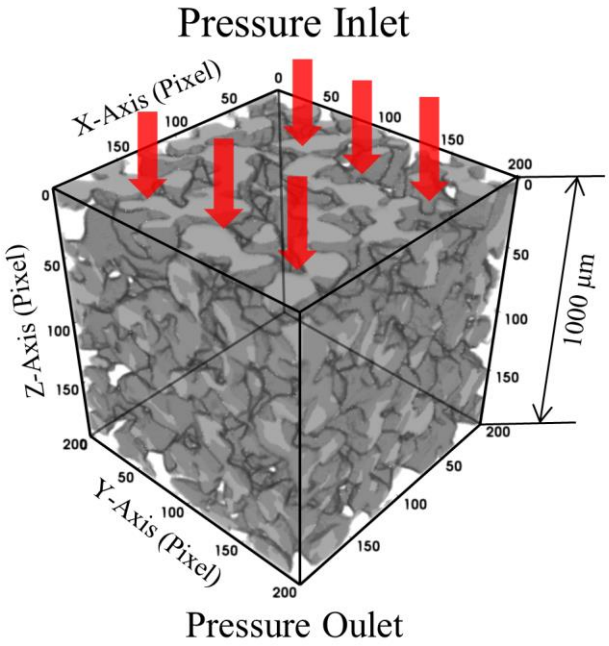

Fig. 5. Boundary conditions for numerical simulation

For the numerical simulation, the binary image was converted into a .DAT-file as needed by PALABOS software to be able to read the entire porous 3D printed sand mold geometry (along with labeled pores and grains), Fig 6. The DAT-file conversion procedure along with the code for MATLAB was used from the tutorial as provided in the PALABOS website by (Degruyter et al., 2010). The code allows for the separation between grains and pores, by creating an interfacial boundary, as shown in Fig. 6(b). Then a constant pressure was imposed at the inlet of the geometry. The bounce-back boundary condition was applied to the interface. Fig. 6(c). shows an example of simulated velocity distribution over a 2D cross-section of an X-ray µ-CT image. *k* was first obtained in non-dimensional lattice units and was then converted to SI units by considering the squared resolution of the original µ-CT image.

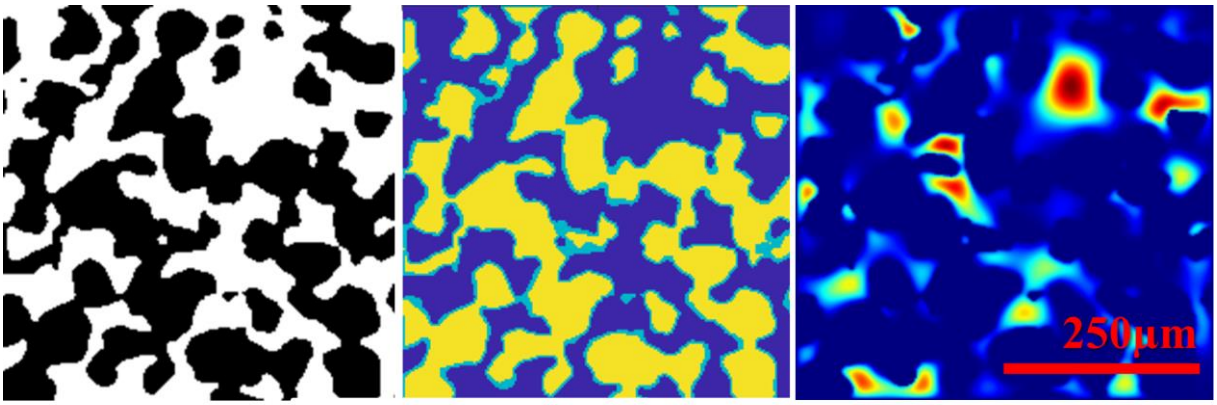

Fig. 6. Visualization of steps in conversion of a µ-CT image for velocity distribution simulation in the case of the SGHB specimen (200 voxels): (a) 2D slice of the binary volume and (b) converted image for simulation with pore space (dark blue pixel), grains (yellow pixel) and grain boundary interface (light blue pixel) where the bounce-back boundary condition is implemented. (c) Simulated velocity distribution through a cross-section.

2.4. Pore network extraction from micro-CT images: pore and throat size distributions

A PNM approach was followed in order to characterize the dimensions of the pore bodies and constrictions of the 3DP molds, by using the images displayed in Fig. 7 as inputs. In the present work, the pores and the throat networks were then extracted from the obtained X-ray µ-CT of the 3DP specimens using the SNOW and GETNET algorithm as shown by (Gostick, 2017). This algorithm was previously implemented on various porous medium ranging from fibrous mats to sandstone, for the extraction of pore and throat sizes, and predicting permeability values. The open-source algorithm called as SubNetwork of the Oversegmented Watershed (SNOW) as provided by (Gostick, 2017) was utilized in the current investigation the extract the pore-network from the X-ray µ-CT images. The extracted pore and throat

445 diameters correspond to the diameter of the largest spheres that can be inscribed in a pore
446 body and a constriction, respectively.

447

448 The method for pore network extraction starts by using GETNET.py code as provided by
449 (Gostick, 2017), which extracts a conventional pore network from the provided µ-CT image
450 of voxel size 200^3. As stated by (Gostick, 2017) the code works in 4 steps, first it extracts the
451 distance map of the pore space (distance transform), secondly a filter was used on the distance
452 map to smoothen the image and to remove the saddles and the plateaus, thirdly merging the
453 peaks that are too close to each other and then lastly assigning the pore space voxel to the
454 appropriate pores using a marker-based watershed algorithm. Recently, (Rodríguez de Castro
455 and Agnaou, 2019) have used the code to extract the pore and throat network of a sandy
456 porous structure. Similarly, for the present extraction, the X-ray µ-CT image of 3DP specimen
457 was first thresholded and then converted into an 8-bit file. Then, using the SNOW algorithm
458 in PYTHON, the X-ray µ-CT image is imported for further characterization. This import class
459 then extracts all the information of the provided µ-CT image, such as pore and throat sizes,
460 their locations and their network connectivity. All pore and throat properties are stored in
461 Numpy arrays, which can be easily accessible at later stage for generating the network.

462

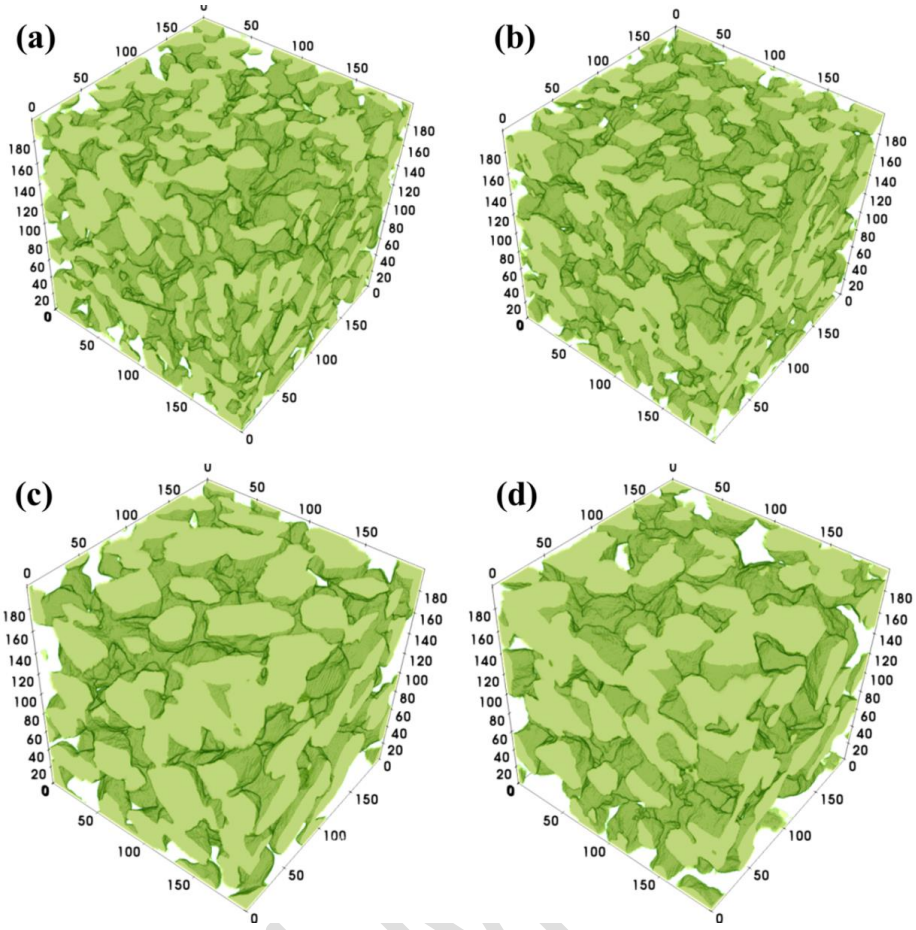

Fig 7. X-ray µ-CT image for all specimens used for PNM, (a) SGLB, (b) SGHB, (c) BGLB and (d) BGHB

Permeability is strongly related to the dimension of the pore constrictions (throats), as most pressure loss is generated in these regions. (Bonnet et al., 2008) studied in detail the effect of form, shape, or structure on flow law properties in metallic foams. On the other hand, (Degruyter et al., 2009) and (Degruyter et al., 2010) showed that the tortuosity (τ), porosity (ε) can be directly correlated according to Archie's law ($\tau^2 = \varepsilon^{-m}$). (Huang et al., 2015) also studied the flow properties within a digital image of fibrous porous medium to predict the permeability and validated the described model. (Degruyter et al., 2009) and (Degruyter et al., 2010) also developed a model to calculate k directly from the characteristic diameter of the throats (d_{throat}) and Archie's law:

$$k = \frac{\varepsilon^{m} d_{throat}^{2}}{32} \quad (8)$$

476

477 The permeability was then calculated by using the average throat size provided by the
478 network model.

479

480 ***2.5. Experimental approach: Local porosity and permeability***

481

482 A detailed review of experimental characterization for density, porosity and permeability
483 method was published recently by (Mitra et al., 2018) and (Mitra et al., 2019), so this section
484 contains only a short description of the method. The weight of the 3D printed specimens was
485 measured using a laboratory precision balance and the density of printed sample was
486 measured as mass divided by volume. The experimentally measured density of 3D printed
487 sand mold was ~1.3 g/cm^3. The particle density is the density of silica sand with ~2.6 g/cm^3.
488 From the measured density of 3DP specimen and silica sand density, the porosity of the 3D
489 printed samples was measured as,

490

$$Porosity\ (\%) = 1 - \frac{Density_{bulk}}{Density_{silica}} \quad (9)$$

491

492 The porosity values measured from experiments were close to 49-51% for all printed
493 specimens, with a standard deviation of 0.25%. Also, the permeability of the 3DP sand mold
494 samples was determined with a permeameter device (Simpson-Electrical), following the
495 recommendations of the American Foundry Society (AFS) and the same procedure presented

in previous works by (Coniglio et al., 2017), (Sivarupan et al., 2017), (Mitra et al., 2018) and (Mitra et al., 2019). Therefore the entire procedure for the permeability experiment will not be presented here. The initial dimensions of the 3D printed parts (cylinders) for experimental gas permeability characterization were of 49.8 ± 0.01 mm in length and of 49.9 ± 0.02 mm in diameter. The relationship for the measurement for gas permeability (GP) is expressed by the following equation:

$$GP = \frac{V \times h}{F \times p \times t} \quad (10)$$

Where V denotes the air volume, h denotes the length of the cylindrical 3DP specimen, F denotes the cross-sectional area of the 3DP specimen, p denotes the pressure and t denotes the passage time for volume of air in minutes. An average permeability value of 5.57×10^{-11} m^2 or ~56.43 Darcy was measured for the small grain (SG) specimens, and 9.02×10^{-11} m^2 or ~91.39 Darcy for the big grain (BG) specimens.

3. Results and discussion

3.1. Grain size distribution and sphericity of silica particles

It is to be noted that since the binder was associated to the solid phase in the CT images, an individual effect of the binder cannot be assessed and therefore the values for low binder and high binder were merged together for the assessment, Fig. 8. The procedure presented in

subsection 2.2.2 was applied to all the segmented X-ray µ-CT images in order to obtain the grain size and sphericity distributions of the silica particles. A normal distribution could be observed for the grain size distribution. The extracted silica grain diameter d_g for small grain specimen varied from ~57 µm to ~331 µm, with mean d_g of ~171.98 µm and the extracted d_g for big grain specimen varied from ~61 µm to ~409 µm, with a mean grain diameter d_g of ~208.05 µm. A more detailed report regarding the granulometry of the 3DP specimens is provided in Table 3, showing the values for high and lower binder contents. GSD has a profound effect on the permeability of the 3DP sand mold. It can be seen that for both small and bigger grains, there is a similar narrow distribution of grain sizes, hence provides good permeability for fabricated 3DP sand mold. Because sand grains with wide range has higher compaction leading to high density and low permeability compared to the narrow distribution.

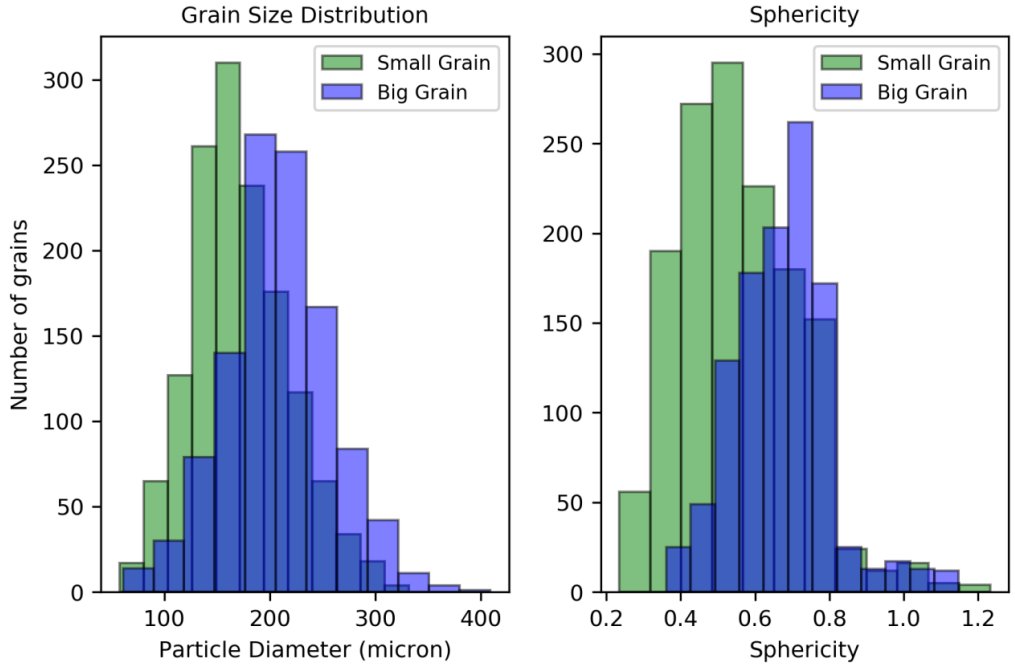

Fig. 8. Combined (a) grain size distribution for small grains and big grains, and (b) sphericity distribution.

Also, the sphericity measured from the X-ray µ-CT image provides information about the particle shape, which affects grain packing density, hence varying porosity and permeability. We note the fact that grains with different shape might have identical sphericity values. The results in terms of sphericity are listed in Table 3. It is observed that the sphericity values of the bigger grain size specimens were higher than those of the small grain size specimens. Some examples of extracted grains from the big grain specimens are shown in Fig. 9. It can be noticed that the grains are far from being a perfect sphere, with an average sphericity value of ~0.6. As we discussed earlier the shape can be rounded, angular, sub-angular, however in the present case, it can be observed that the grains are mostly sub-angular. All the results of the sphericity of the specimens are shown as a histogram in Fig. 8.

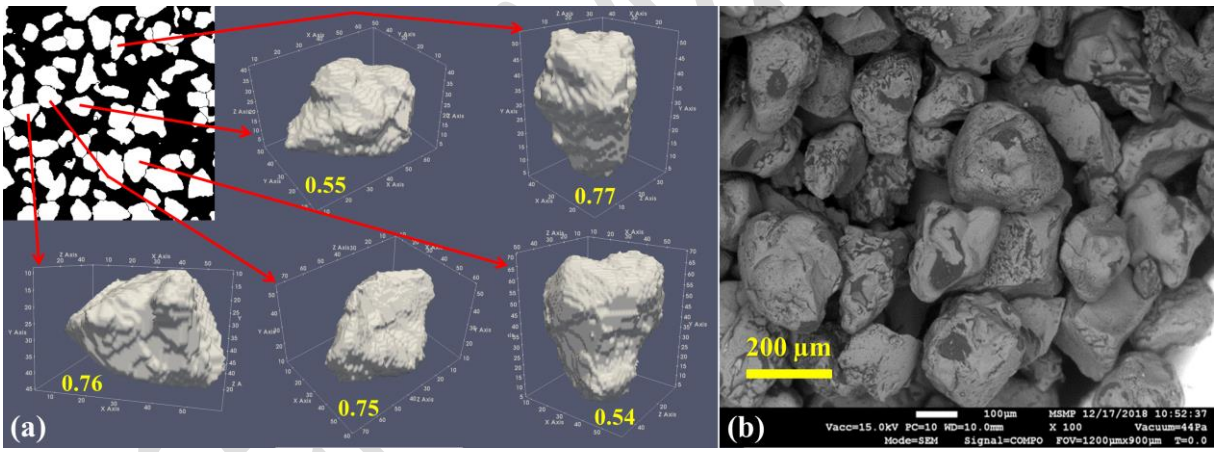

Fig. 9. (a) Examples of silica grain with different sphericity number in the BG specimen. (b) SEM image of a 3DP specimen, showing the silica grains.

From the obtained granulometry, using the porosity and mean grain diameter, the permeability of the 3DP specimens were predicted with the Kozeny-Carman equation (Eq. 3) as shown in Table 3. It is to be noted that since the binder was associated to the solid phase in

the CT images, an individual effect of the binder cannot be assessed and therefore the values for low binder and high binder are very close.

Table 3. Results from image analysis

Sample Type	Mean d_g (µm)	Mean Sphericity	Mean porosity (%)	Permeability (m^2)	Permeability (Darcy)
SGLB	154.07	0.56	50.97	6.593×10^{-11}	66.80
SGHB	156.85	0.55	49.37	6.182×10^{-11}	62.63
BGLB	210.11	0.66	48.48	1.003×10^{-10}	101.62
BGHB	207.04	0.67	49.35	1.077×10^{-10}	109.12

3.2. Permeability of the printed samples as obtained from LBM numerical simulations

The steady-state velocity maps provided by the LBM simulations introduced in subsection 2.3., throughout the simulated specimens were represented using PARAVIEW software as shown in Fig. 10. It can be deduced from this figure that the velocity distribution is not uniform throughout the porous media, as expected due to the varying cross-section dimensions of the interstices. The ratio between pressure difference (ΔP) and the volumetric flow rate was constant for all the tested values of ΔP, confirming creeping regime. Different image sizes (50^3 voxel, 100^3 voxel, 150^3 voxel, and 200^3 voxel) were used in the simulations for the computation of k. Table 4 provides the permeability values for all the specimens as provided by LBM solver PALABOS by using the modified Darcy's equation (Eq. 7) as stated earlier in section 2.3. Indeed, from Fig. 11, it can be observed that the permeability value for

567 50 voxel image is lower than that of 100 voxel, 150 voxel and 200 voxel image stack for all
568 the 3DP specimens. The permeability values approached a plateau value when the size of the
569 RVE was greater than 100 voxels. Therefore, it is suggested to use an input volume of 500
570 μm^3, which corresponds to the size of 3 equivalent layers (3×190 µm or 3×140 µm) of silica
571 grains for 3DP specimens with average grain diameter of 140 µm and 190 µm. Bigger image
572 sizes would lead to higher simulation times without any significant improvement in accuracy.

573

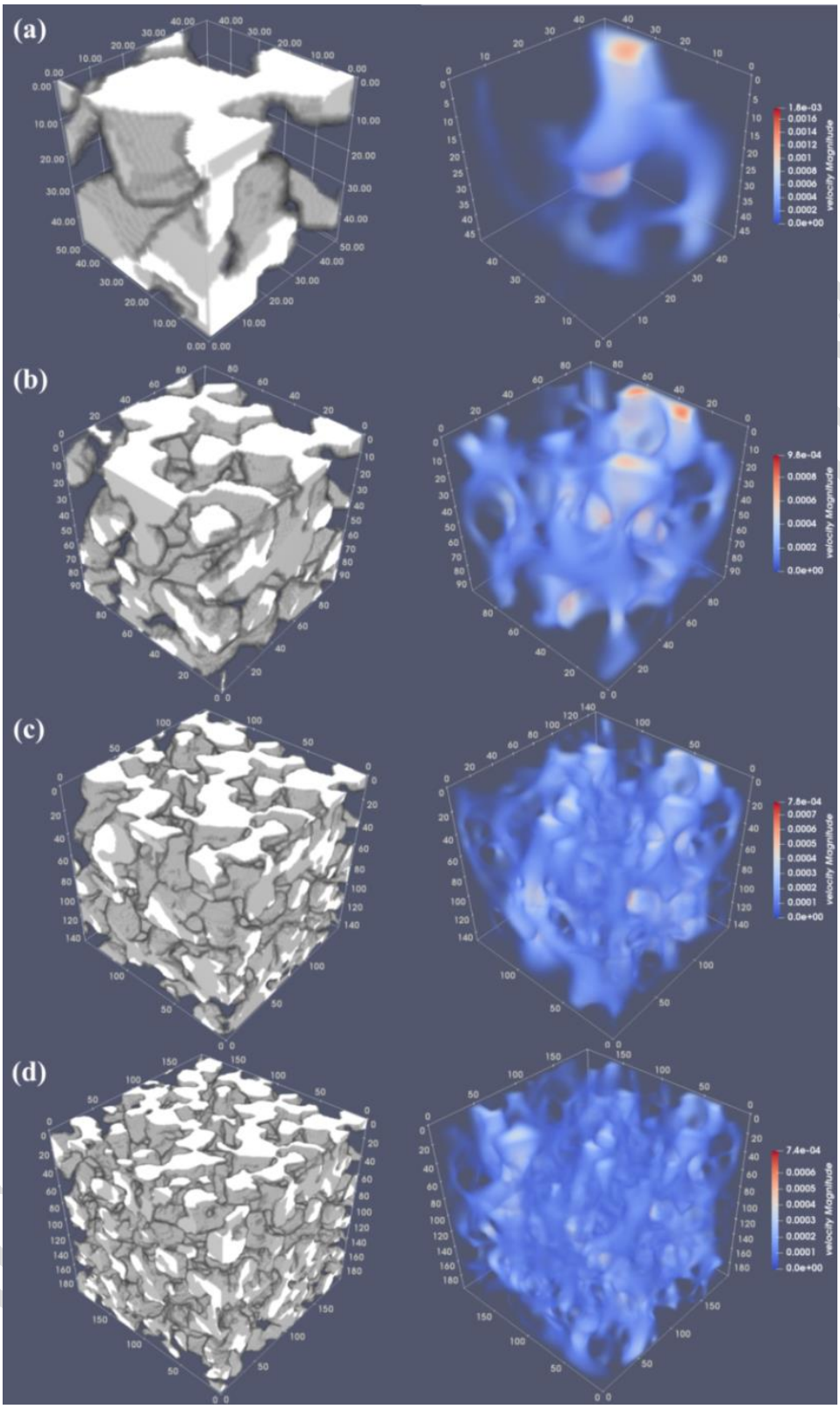

574

575 **Fig. 10.** Velocity map in lattice units through specimens of, (a) 50, (b) 100, (c) 150, and (d)

576 200 voxel. (Warmer colors represent higher velocity)

577

578 **Table 4.** Results from permeability simulation

Image Size (voxel)	Porosity (%)	Permeability (m^2)	Permeability (Darcy)
Small Grain Low Binder (SGLB)			
50	51	4.431×10^{-11}	44.89
100	50	4.844×10^{-11}	49.08
150	51	5.215×10^{-11}	52.84
200	52	4.842×10^{-11}	49.06
Small Grain High Binder (SGHB)			
50	49	4.403×10^{-11}	44.61
100	51	5.475×10^{-11}	55.47
150	50	5.077×10^{-11}	51.44
200	53	5.166×10^{-11}	52.34
Big Grain Low Binder (BGLB)			
50	49	3.889×10^{-11}	39.41
100	51	8.801×10^{-11}	89.17
150	49	8.788×10^{-11}	89.04
200	52	9.092×10^{-11}	92.12
Big Grain High Binder (BGHB)			
50	49	4.171×10^{-11}	42.26
100	52	9.157×10^{-11}	92.78
150	53	9.027×10^{-11}	91.46
200	53	9.189×10^{-11}	93.11

579

580

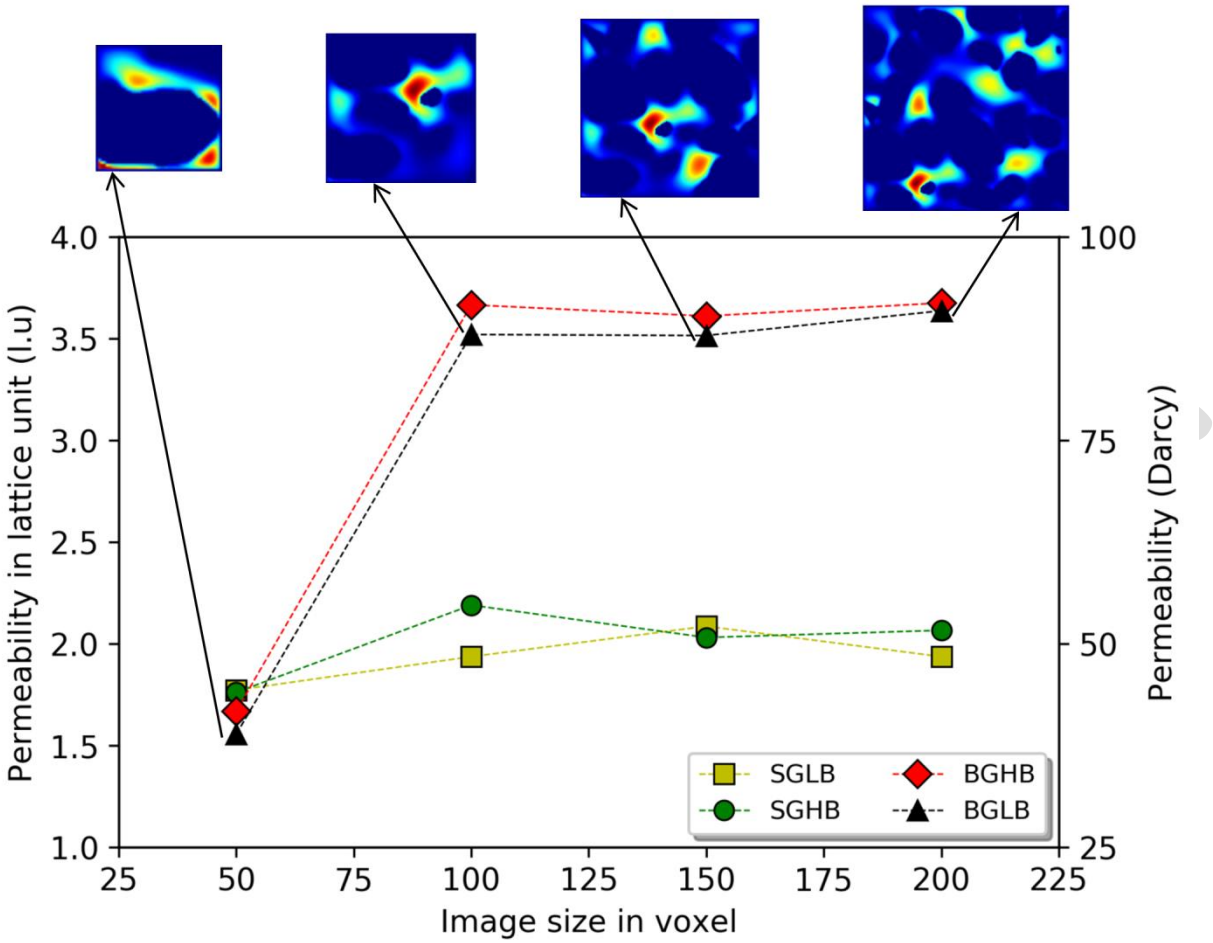

581

582 **Fig. 11.** Effect of input geometry volume on the computed value of permeability

583

584 The computed results of permeability for 3DP specimen through PALABOS with different
585 grain and binder percent samples can be compared with the predicted analytical results and
586 image analysis results. The agreement is good between the analytical method, the image
587 analysis and the experimental results for all the 3DP specimens (SGLB, SGHB, BGLB, and
588 BGHB). The permeability calculations obtained with PALABOS are in good co-relation with
589 the experimental measurements performed with the 3DP specimen, as shown in Table 4.
590 Although it is of worth mentioning that an analytical permeability value of 4.9×10^{-11} m^2 (or)
591 ~49 Darcy was calculated with Kozeny-Carmen equation (Eq 3), by using the average grain
592 size of 140 micron (as provided by the ExOne sand provider) and measured porosity of 49.2

%. And also a permeability of 9.071×10^{-11} m^2 (or) ~91 Darcy was calculated) with the average grain size of 190 micron (as provided by the ExOne sand provider) and measured porosity of 49.5 %. A deviation of permeability could be observed compared to analytical permeability value as the prediction of Kozeny-Carmen is based on the particles being a perfect sphere (the equation uses the mean diameter, ds), whereas in the present scenario the particle is close to being a perfect sphere (average sphericity = 0.65). The analytically predicted permeability value using Kozeny-Carmen equation worked as a reference for the permeability measurements. It can be observed from the table that, it is possible to predict the absolute permeability of 3DP sand mold using the non-destructive LBM simulation and is a very strong method for mass flow simulation in complex 3D printed sand mold.

3.3. Pores and Throats Size Distributions of the 3D printed samples as provided by pore-network modeling

PNM provides a reasonable prediction of mass transport properties at pore scale and offers the flexibility of characterizing macroscopic properties relationship of 3DP sand mold with pore structure. With PNM, the complex pore structure of a 3DP sand mold can be represented by a network of pores (pore spaces) and connected throats (narrow paths that connect pores) with simplified geometries. A pore network modeling aims at better representation of pore and throat interconnectivity in a porous medium like 3DP sand mold. All the pore network extractions for different specimens (SGLB, SGHB, BGLB, BGHB) were performed over a µ-CT image size of 200^3 voxel with a resolution of 5 µm per voxel, and are represented in Fig. 12.

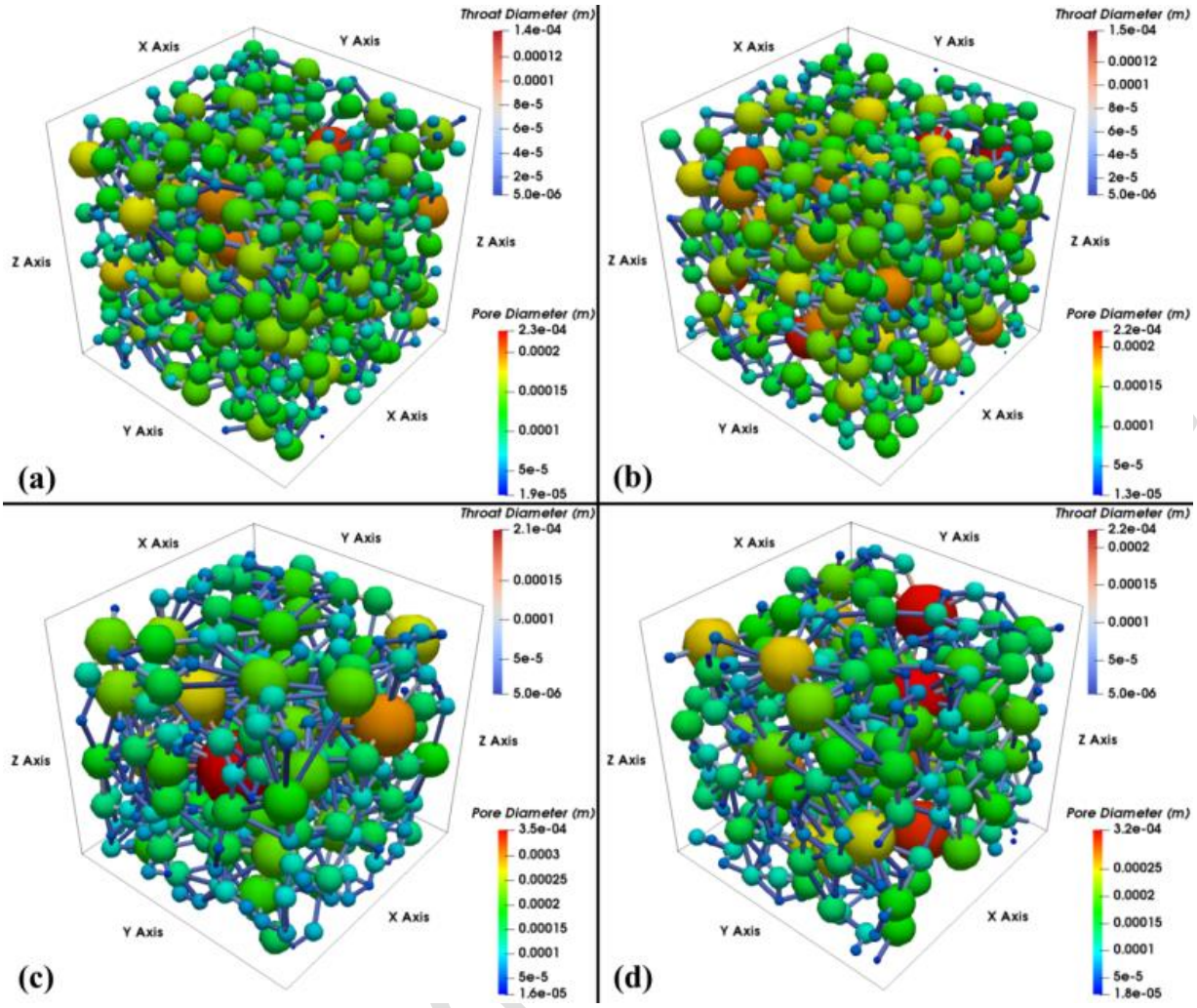

Fig. 12. Extracted pore network for (a) SGLB, (b) SGHB, (c) BGLB and (d) BGHB specimens.

The pore-size distributions (PSDs) in terms of pore diameter were extracted from the generated pore network and are represented as a histogram, Fig. 13. The extracted pore diameter for SGLB specimen varied from ~19 µm to ~226 µm, with a mean pore diameter of ~105.84 µm and the extracted pore diameter for SGHB specimen varied from ~14 µm to ~220 µm, with a mean pore diameter of 108.05 µm. Similarly, the extracted pore diameter for BGLB specimen varied from ~16 µm to ~350 µm, with a mean pore diameter of 108.07 µm and the extracted pore diameter for BGHB specimen varied from ~18 µm to ~320 µm, with a

mean pore diameter of ~108.31 µm. Although previous work by (Glover and Walker, 2009) showed that the grain size and pore radius are functionally interdependent, it can be observed that the average pore diameters are very similar for all the specimens (both SG and BG) in the currently investigated samples. However, careful observation of Fig. 13 shows that the standard deviation of the PSD is considerably higher for the big sand grains samples (± 55.9 µm for BGLB and ± 56.1 µm for BGHB) as compared to the small sand grains samples (± 37.3 µm for SGLB and ± 38.7 µm for SGHB). Consequently, the size of the biggest pores in the big grain samples is much higher than for the small grain samples, even if the average pore size is close in both cases. This can be also observed in the red-colored pores of Fig. 12 (approximately 350 micrometers of big grains and 230 for small grains) and in the PSDs provided in Figure 13.

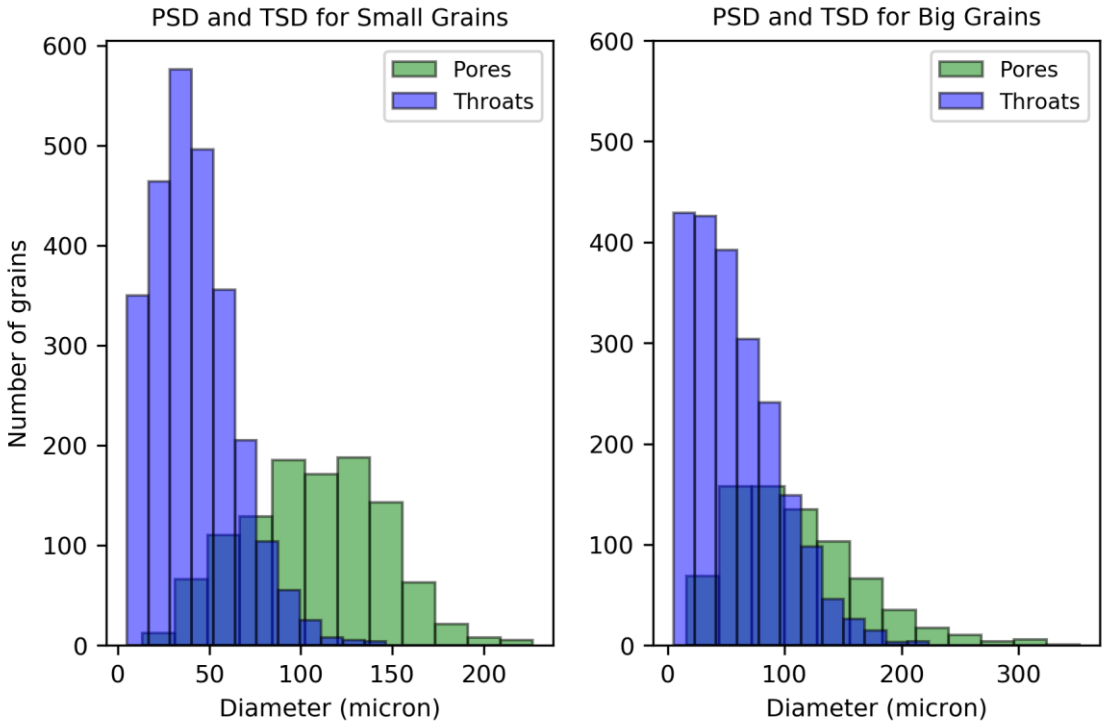

Fig. 13. Combined (high binder +low binder) pore size and throat size distribution for (a) small grains and (b) big grains.

643

644 The throat-size distributions (TSDs) in diameter were also extracted from the generated throat
645 network and were then represented as a cumulative histogram with the throat diameter, Fig.
646 13. The extracted throat diameter for SGLB specimen varied from ~5 μm to ~140 μm, with a
647 mean throat diameter of 38.66 μm and the extracted throat diameter for SGHB specimen
648 varied from ~5 μm to ~146 μm, with a mean throat diameter of 44.43 μm. Similarly, the
649 extracted throat diameter for BGLB specimen varied from ~5 μm to ~214 μm, with a mean
650 throat diameter of 56.92 μm and the extracted throat diameter for BGHB specimen varied
651 from ~5 μm to ~220 μm, with a mean throat diameter of 58.42 μm. It can be depicted from
652 the distribution that, the peak values for both cases appear to be near low pore sizes, which
653 defines the microstructure complexity. It can also be observed for big grain specimens that the
654 throats and pores overlap with each other, which suggests that there exist some small pores,
655 which are of similar size as that of the throats. Moreover, the distribution of throat size for all
656 the specimens shows a right-skewed distribution, along with a quantitatively great portion of
657 the small size throats (peak throat size smaller than average), which construct minor flow
658 paths.

659

660 **Table 5.** Results from pore network modeling

Sample Type	Mean Pore Diameter (μm)	Mean Throat Diameter (μm)	Permeability (m^2)	Permeability (Darcy)
SGLB	105.84	38.66	3.138×10^{-11}	31.79
SGHB	108.05	44.43	4.144×10^{-11}	41.98
BGLB	108.07	56.92	6.915×10^{-11}	70.06
BGHB	108.31	58.42	7.165×10^{-11}	72.59

From the obtained average equivalent throat diameter and tortuosity, permeability was calculated using the equation described in the previous section, Eq. 8, and the results are presented in Table 5. It can be observed from the results that no significant differences in terms of permeability (k) were obtained for small grain samples with different binder content along with big grain samples with different binder content, as the furan resin binder was only associated to the solid phase in the µ-CT images. An individual effect of the binder over pore network structure cannot be assessed and therefore the values for pore and throat diameter for samples with low binder and high binder are very close.

4. Model efficiency

One of the challenges in foundry is the lack of methods for proper non-destructive characterization of the local permeability of the 3DP sand mold. The X-ray µCT technique overcomes this challenge and allows a non-destructive visualization and characterization of internal volume and the external surface of a sand mold. This paper, for the first time, fully characterizes the intrinsic physical parameters of 3DP sand mold including grain structure, porosity, pore connectivity, tortuosity, pore size distribution, throat size distribution and local density. Table. 6 shows the cumulative results of permeability as obtained by different methods (from traditional experiment, from GSD, from LBM and from PNM). The permeability value using the GSD method overpredicts the permeability value as obtained with the traditional experiments. Indeed, the permeability value from GSD using Kozeny-Carman equation is based on the particles being a perfect sphere (the equation uses the mean particle diameter, d_s), whereas in the present scenario the particle is close to being a perfect

sphere (average sphericity = 0.65). However, the permeability value obtained with GSD using Kozeny-Carman equation can still be considered as a reference for other models.

Moreover, the permeability values yielded by LBM simulations were found to be close to the results provided by traditional tests. Nevertheless, LBM requires much computational power for larger µ-CT images, hence this method can be time consuming. Therefore, it was crucial to identify the optimum RVE not only to predict reliable permeability values but also to reduce simulation times. An alternative approach to predict permeability from pore-network modelling (PNM) is proposed. Pores are the relatively wide portions of the interstices and throats are the relatively narrow portions that separate the pore bodies. The pores and throats space of a 3D printed sand mold can be extracted from the segmented 3D µ-CT image. As can be observed from Table 6, significant differences are reported in some cases between the results of traditional experiments and PNM, while the agreement is better between traditional tests and GSD and LBM. Nevertheless, as compared to LBM simulations, PNM require less computational power due to the simplifications of the void-space geometry and topology when constructing the pore network model. The computational time needed for the extraction of the pore and throat network on a computer with Intel Xeon processor and 16 GB of memory is in the order of minutes, whereas using LBM computation takes hours. This allows the computation of permeability over larger sampling volumes. However, it should be noted that the computational time can be significantly reduced by using a more powerful and expensive supercomputer. (Chauveteau et al., 1996) showed that for unconsolidated porous media where pore throats are much smaller than pore bodies, the viscous dissipation can be considered as being localized only in pore throats. This approximation is quite acceptable in many cases, since the pore body-to-pore throat radius is generally quite large, varying from values around 3 for random monosized sphere packs, to around 5 for random packs of sharp-

edged grains with a narrow size distribution. However, in the case of the highly-porous 3DP sand molds investigated in the present work, the pore-to-throat size ratios range from ~1.7 to ~2.7 (Table 5). Therefore, the PNM-based estimation obtained with Eq. 8, in which viscous dissipation is assumed to be localized only in pore throats, is not expected to be highly accurate, but is still useful to provide a lower permeability bound. Hence, PNM approach can be a reasonable alternative to the traditional experimental, LBM and GSD methods as it takes into account of the microstructural features of the 3DP sand mold and can also easily deal with any kind of complex geometry.

Table 6. Permeability measured with different methods

Sample	Traditional experiment (Darcy)	GSD (Darcy)	LBM using 100 voxel (Darcy)	PNM (Darcy)
SGLB	56.4	66.8	49	31.79
SGHB	58.9	62.6	55.4	41.98
BGLB	91.3	101.6	89.1	70.06
BGHB	93.2	109.1	92.7	72.59

Permeability, porosity, tortuosity grain size distribution, pore size distribution, average pore diameter, throat size distribution, and average throat diameter are essential inputs when predicting gas flow in 3DP molds. It is to be noted that complex porous media like 3DP sand mold have anisotropic properties (mechanical and mass transport) due to variation in printing process parameters. For the present study, only the variation of furan resin binder droplet resolution on silica sand powder bed is studied (different binder percentage) along with different silica grain size, as this affects the properties of complex porous resin bonded 3DP

mold with the recoater speed. The present modeling approaches are advantageous on the prediction of the flow permeability of such complex porous structure like 3DP sand mold directly from the from X-Ray µ-CT digital images. This would help the foundry industry to accurately measure the mass transport properties as required as an input for numerical simulations (solidification and filling), to study the effect of printing process parameters (printing speed, binder percentage, grain size, etc.) and thermal degradation of furan resin binder during metal casting. Therefore, the present approaches of merging permeability measurements on 3DP sand mold specimens with extraction of throat and pore network structure using for X-ray µ-CT helped in exploring and better understanding the pore construction and its pivotal role on mass flow phenomenon. It also helped us in developing and validating reliable models for non-destructive prediction of gas permeability, which are favorable for carrying out precise risk assessments of harmful toxic pollutants produced during metal casting in foundry industry.

5. Conclusion

Permeability is one of the most important factors affecting the generation of gas defects during metal casting, so it is of major importance to characterize it. In this work, the advantage of the application of X-ray µ-CT (NDT), Pore Network Modelling methods and Lattice Boltzmann Method in exploring the mass transport properties of additively processed silica sand mold was demonstrated. X-ray µ-CT images were used to compute the porosity, pore size, throat size and the permeability of the 3D printed specimens for different binder contents and grain sizes, using analytical and numerical methods. The permeability predicted in the steady-state was compared with experimental and analytical measurements for layered

752 silica grain arrangement. A major advantage of using X-ray CT characterization is the non-
753 destructive nature of the tests. The computed permeability can be used as input to numerical
754 simulations of metal casting allowing the prediction of macroscopic defects. The following
755 scientific and industrial implications are drawn from the present work:

756

757 • The permeability values predicted with LBM from X-ray µ-CT image of 3DP specimen
758 are in good agreement with the traditional experimental measurements.

759

760 • The proposed non-destructive X-ray µ-CT technique is an effective and reliable
761 alternative to traditional laboratory experiments for permeability characterization of
762 additively processed sand molds. The good agreement between the analytical model,
763 traditional experimental estimations and the proposed method based on CT data validates
764 this approach.

765

766 • An RVE of 100×100×100 voxel corresponding to 500×500×500 μm^3 is suggested for a
767 faster and reliable permeability simulation.

768

769 • The characterization of the 3D printed specimen was performed by using available open-
770 source software such as ImageJ, Palabos, and OpenPNM and therefore the proposed
771 approach may be used in a broad range of academic or research applications.

772

773 • The permeability value predicted using pore network modeling can be a reasonable
774 alternative as it takes into account of the microstructural features of the 3DP sand mold.

775

The present findings represent a step forward towards improved prediction of mass transport properties of the 3DP sand molds. However, further characterization of permeability of such additively processed sand mold should be performed with varying average grain diameter, to check the convergence of the present model. Also samples printed with other printing process parameters should be studied.

6. Acknowledgment

The assistance of Mr. Jérémie Bourgeois with the 3D printing of sand specimens is greatly appreciated.

References

Almaghariz, E.S., 2015. Determining When to Use 3D Sand Printing : Quantifying the Role of Complexity By Eyad S . Almaghariz A thesis Submitted in Partial Fulfillment of the Requirements for the Degree of Master of Science in the.

Almaghariz, E.S., Conner, B.P., Lenner, L., Gullapalli, R., Manogharan, G.P., Lamoncha, B., Fang, M., 2016. Quantifying the role of part design complexity in using 3d sand printing for molds and cores. Int. J. Met. 10, 240–252. https://doi.org/10.1007/s40962-016-0027-5

Anbar, S., Thompson, K.E., Tyagi, M., 2019. The Impact of Compaction and Sand Migration on Permeability and Non-Darcy Coefficient from Pore-Scale Simulations. Transp. Porous Media 127, 247–267. https://doi.org/10.1007/s11242-018-1190-3

Auzerais, F.M., Dunsmuir, J., Ferréol, B.B., Martys, N., Olson, J., Ramakrishnan, T.S., Rothman, D.H., Schwartz, L.M., 1996. Transport in sandstone: A study based on three dimensional microtomography. Geophys. Res. Lett. 23, 705–708. https://doi.org/10.1029/96GL00776

Ayachit Utkarsh, 2015. The ParaView Guide: A Parallel Visualization Application, Kitware.

Boek, E.S., Venturoli, M., 2010. Lattice-Boltzmann studies of fluid flow in porous media with realistic rock geometries. Comput. Math. with Appl. 59, 2305–2314. https://doi.org/10.1016/j.camwa.2009.08.063

Bonnet, J.P., Topin, F., Tadrist, L., 2008. Flow laws in metal foams: Compressibility and pore size effects. Transp. Porous Media 73, 233–254. https://doi.org/10.1007/s11242-007-9169-5

Boulos, V., Fristot, V., Houzet, D., Salvo, L., Lhuissier, P., 2013. Investigating performance variations of an optimized GPU-ported granulometry algorithm To cite this version : Investigating performance variations of an optimized GPU-ported granulometry algorithm. Des. Archit. Signal Image Process. (DASIP), 2012 Conf. on, Oct 2012, Karlsruhe, Ger. 1–6.

Chauveteau, G., Nabzar, L., El Attar, Y., Jacquin, C., 1996. Pore Structure and Hydrodynamics, in: SCA Conference Paper Number 9607.

Chopard B, Dupuis A, Masselot A, Luthi P, 2002. Cellular Automata and Lattice Boltzmann techniques: an approach to model and simulate complex systems. Adv. Complex Syst. 05, 101–102. https://doi.org/10.1142/S0219525902000560

Coniglio, N., Sivarupan, T., El Mansori, M., 2017. Investigation of process parameter effect on anisotropic properties of 3D printed sand molds. Int. J. Adv. Manuf. Technol. https://doi.org/10.1007/s00170-017-0861-5

De Chiffre, L., Carmignato, S., Kruth, J.P., Schmitt, R., Weckenmann, A., 2014. Industrial applications of computed tomography. CIRP Ann. - Manuf. Technol. 63, 655–677. https://doi.org/10.1016/j.cirp.2014.05.011

Degruyter, W., Bachmann, O., Burgisser, A., 2009. Controls on magma permeability in the volcanic conduit during the climactic phase of the Kos Plateau Tuff eruption (Aegean Arc). Bull. Volcanol. 72, 63–74. https://doi.org/10.1007/s00445-009-0302-x

Degruyter, W., Burgisser, A., Bachmann, O., Malaspinas, O., 2010. Synchrotron X-ray microtomography and lattice Boltzmann simulations of gas flow through volcanic pumices. Geosphere 6, 470–481. https://doi.org/10.1130/GES00555.1

Ding, W.T., Xu, W.J., 2018. Study on the multiphase fluid-solid interaction in granular

materials based on an LBM-DEM coupled method. Powder Technol. 335, 301–314. https://doi.org/10.1016/j.powtec.2018.05.006

ExOne, 2014. FB001 (Furan Binder) - Fiche De Données De Sécurité Caprolactam,selon 1907/2006/CE, Article 31.

ExOne, 2013. FS001 (Silica sand)-Material data sheet.

Ferrol, B., Rothman, D.H., 1995. Lattice-Boltzmann simulations of flow through Fontainebleau sandstone. Transp. Porous Media 20, 3–20. https://doi.org/10.1007/BF00616923

FLANNERY, B.P., DECKMAN, H.W., ROBERGE, W.G., D'AMICO, K.L., 1987. Three-Dimensional X-ray Microtomography. Science (80-.). 237, 1439–1444. https://doi.org/10.1126/science.237.4821.1439

Glover, P.W.J., Walker, E., 2009. Grain-size to effective pore-size transformation derived from electrokinetic theory. Geophysics 74. https://doi.org/10.1190/1.3033217

Gostick, J., Aghighi, M., Hinebaugh, J., Tranter, T., Hoeh, M.A., Day, H., Spellacy, B., Sharqawy, M.H., Bazylak, A., Burns, A., Lehnert, W., Putz, A., 2016. OpenPNM: A Pore Network Modeling Package. Comput. Sci. Eng. 18, 60–74. https://doi.org/10.1109/MCSE.2016.49

Gostick, J.T., 2017. Versatile and efficient pore network extraction method using marker-based watershed segmentation. Phys. Rev. E 96, 1–15. https://doi.org/10.1103/PhysRevE.96.023307

Hawaldar, N., Zhang, J., 2018. A comparative study of fabrication of sand casting mold using additive manufacturing and conventional process. Int. J. Adv. Manuf. Technol. 97,

1037–1045. https://doi.org/10.1007/s00170-018-2020-z

Hazlett, R.D., 1995. Simulation of capillary-dominated displacements in microtomographic images of reservoir rocks. Transp. Porous Media 20, 21–35. https://doi.org/10.1007/BF00616924

Hecht, M., Harting, J., 2008. Implementation of on-site velocity boundary conditions for D3Q19 lattice Boltzmann 1–14. https://doi.org/10.1088/1742-5468/2010/01/P01018

Heijs, A.W.J., Lowe, C.P., 1995. Numerical evaluation of the permeability and the Kozeny constant for two types of porous media. Phys. Rev. E 51, 4346–4352. https://doi.org/10.1103/PhysRevE.51.4346

Hormann, K., Baranau, V., Hlushkou, D., Höltzel, A., Tallarek, U., 2016. Topological analysis of non-granular, disordered porous media: Determination of pore connectivity, pore coordination, and geometric tortuosity in physically reconstructed silica monoliths. New J. Chem. 40, 4187–4199. https://doi.org/10.1039/c5nj02814k

Huang, X., He, Y., Zhou, W., Deng, D., Zhao, Y., 2019. Pore network modeling of fibrous porous media of uniform and gradient porosity. Powder Technol. 343, 350–361. https://doi.org/10.1016/j.powtec.2018.11.022

Huang, X., Wang, Q., Zhou, W., Deng, D., Zhao, Y., Wen, D., Li, J., 2015. Morphology and transport properties of fibrous porous media. Powder Technol. 283, 618–626. https://doi.org/10.1016/j.powtec.2015.06.015

Ignacio Arganda-Carreras, Rodrigo Fernandez-Gonzalez, Arrate Munoz-Barrutia, Carlos Ortiz-De-Solorzano, 2010. 3D reconstruction of histological sections: Application to mammary gland tissue. Microsc. Res. Tech. 73, 1019–1029.

885 Jaganathan, S., Vahedi Tafreshi, H., Pourdeyhimi, B., 2008. A realistic approach for modeling
886 permeability of fibrous media: 3-D imaging coupled with CFD simulation. Chem. Eng.
887 Sci. 63, 244–252. https://doi.org/10.1016/j.ces.2007.09.020

888 Kadauw, A., 2014. Characterization of the parameters of sand moulds in compaction process
889 by use of the industrial computer tomography (ICT). Arch. Metall. Mater. 59, 1097–
890 1101. https://doi.org/10.2478/amm-2014-0189

891 Latt J, 2009. Palabos, Parallel Lattice Boltzmann Solver: http://www.lbmethod.org/palabos/.

892 Legland, D., Arganda-Carreras, I., Andrey, P., 2016. MorphoLibJ: Integrated library and
893 plugins for mathematical morphology with ImageJ. Bioinformatics 32, 3532–3534.
894 https://doi.org/10.1093/bioinformatics/btw413

895 Malaspinas, O., Fiétier, N., Deville, M., 2010. Lattice Boltzmann method for the simulation of
896 viscoelastic fluid flows. J. Nonnewton. Fluid Mech. 165, 1637–1653.
897 https://doi.org/10.1016/j.jnnfm.2010.09.001

898 Mitra, S., Rodríguez de Castro, A., El Mansori, M., 2019. On the rapid manufacturing process
899 of functional 3D printed sand molds. J. Manuf. Process. 42, 202–212.
900 https://doi.org/10.1016/j.jmapro.2019.04.034

901 Mitra, S., Rodríguez de Castro, A., El Mansori, M., 2018. The effect of ageing process on
902 three-point bending strength and permeability of 3D printed sand molds. Int. J. Adv.
903 Manuf. Technol. 97, 1241–1251. https://doi.org/10.1007/s00170-018-2024-8

904 Ramezani Dana, H., El Mansori, M., 2019. Etude du comportement mécanique d'une
905 structure poreuse obtenue par impression 3D au sable, in: 24ème Congrès Français de
906 Mécanique.

907 Rodríguez de Castro, A., Agnaou, M., 2019. Numerical Investigation of the Apparent
908 Viscosity Dependence on Darcy Velocity During the Flow of Shear-Thinning Fluids in
909 Porous Media. Transp. Porous Media. https://doi.org/10.1007/s11242-019-01279-x

910 Sachs, E., Cima, M., Cornie, J., 1990. Three-dimensional printing: rapid tooling and
911 prototypes directly form a CAD model. CIRP Ann. - Manuf. Technol. 39, 201–204.
912 https://doi.org/http://dx.doi.org/10.1016/S0007-8506(07)61035-X

913 Schindelin, J., Arganda-Carreras, I., Frise, E., Kaynig, V., Longair, M., Pietzsch, T.,
914 Preibisch, S., Rueden, C., Saalfeld, S., Schmid, B., Tinevez, J.Y., White, D.J.,
915 Hartenstein, V., Eliceiri, K., Tomancak, P., Cardona, A., 2012. Fiji: An open-source
916 platform for biological-image analysis. Nat. Methods 9, 676–682.
917 https://doi.org/10.1038/nmeth.2019

918 Sivarupan, T., El Mansori, M., Daly, K., Mavrogordato, M.N., Pierron, F., 2018.
919 Characterisation of 3D printed sand moulds using micro-focus X-ray computed
920 tomography. Rapid Prototyp. J. https://doi.org/10.1108/RPJ-04-2018-0091

921 Sivarupan, T., ElMansori, M., Coniglio, N., 2017. 3D Printing Process Parameters and
922 Properties of Additively Manufactured Sand Mold for Rapid Casting : Strength and
923 Permeability. Addit. Manuf. (under review).

924 Smith, P., Reid, D.B., Environment, C., Palo, L., Alto, P., Smith, P.L., 2010. A Threshold
925 Selection Method from Gray-Level Histograms C, 62–66.

926 Soulaine, C., 2015. Direct numerical simulation in fully saturated porous media. Stanford.Edu
927 1–27.

928 Thabet, A., Straatman, A.G., 2018. The development and numerical modelling of a
929 Representative Elemental Volume for packed sand. Chem. Eng. Sci. 187, 117–126.

https://doi.org/10.1016/j.ces.2018.04.054

Upadhyay, M., Sivarupan, T., El Mansori, M., 2017. 3D Printing for Rapid Sand Casting - A Review. J. Manuf. Process. 29, 211–220. https://doi.org/10.1016/j.jmapro.2017.07.017

Xiong, Q., Baychev, T.G., Jivkov, A.P., 2016. Review of pore network modelling of porous media: Experimental characterisations, network constructions and applications to reactive transport. J. Contam. Hydrol. 192, 101–117. https://doi.org/10.1016/j.jconhyd.2016.07.002